Material-informed Gaussian Splatting for 3D World Reconstruction in a Digital Twin

Andy Huynh^{1,2,*}, João Malheiro Silva^{1,*}, Tong Duy Son¹, and Holger Caesar²

Abstract-3D reconstruction for Digital Twins often relies on LiDAR-based methods, which provide accurate geometry but lack the semantics and textures naturally captured by cameras. Traditional LiDAR-camera fusion approaches require complex calibration and still struggle with certain materials like glass, which are visible in images but poorly represented in point clouds. We propose a camera-only pipeline that reconstructs scenes using 3D Gaussian Splatting from multi-view images, extracts semantic material masks via vision models, converts Gaussian representations to mesh surfaces with projected material labels, and assigns physics-based material properties for accurate sensor simulation in modern graphics engines and simulators. This approach combines photorealistic reconstruction with physics-based material assignment, providing sensor simulation fidelity comparable to LiDAR-camera fusion while eliminating hardware complexity and calibration requirements. We validate our camera-only method using an internal dataset from an instrumented test vehicle, leveraging LiDAR as ground truth for reflectivity validation alongside image similarity metrics.

Index Terms—3D Reconstruction, Computer Vision, Digital Twin, Gaussian Splatting, Material Segmentation, Physics-Based Rendering, Sensor Simulation

I. INTRODUCTION

Digital Twins are integral to advancing sensor technologies, facilitating the safe validation of high-risk scenarios and precise control over environmental variables prior to real-world deployment. Modern Advanced Driver Assistance Systems (ADAS) and Artificial Intelligence (AI) systems rely on sophisticated algorithms and complex multimodal sensor setups, often including LiDAR sensors and cameras. Achieving accurate translation of real-world scenarios to simulation—where virtual sensors exhibit identical behavior to their physical counterparts—requires 3D world reconstruction that captures spatial and geometric features to ensure realistic simulation and synthetic sensor data consistent with reality.

Previous LiDAR-based approaches [34, 17] have achieved accurate geometric reconstruction for static scenes but lack the texture information naturally captured by cameras, limiting

photorealistic rendering capabilities. Moreover, LiDAR struggles with transparent and reflective materials such as glass and metal, which are readily captured in camera images but produce inaccurate point clouds. While incorporating material properties into LiDAR-based reconstruction has been shown to improve sensor simulation accuracy [19], such approaches still require LiDAR hardware and do not address texture acquisition. Combining LiDAR with cameras to capture both geometry and appearance requires complex sensor synchronization and calibration procedures, yet still produces limited texture quality under sparse-view conditions, as traditional reconstruction methods struggle to generate photorealistic results.

Recent advancements in novel view synthesis have introduced 3D Gaussian Splatting [12], an efficient technique providing fast, differentiable rendering and high-quality reconstructions from sparse input views. While originally focused on photorealistic rendering, recent works such as MILo [8] have shown that geometric surfaces can be extracted from Gaussian Splatting using only multi-view images, enabling a hybrid representation where Gaussian Splatting provides photorealistic visualization while extracted meshes enable physics-based simulation in modern graphics engines. These cameraonly methods provide an alternative to LiDAR hardware, avoiding intricate sensor synchronization and demanding calibration procedures while delivering superior texture quality.

Building on these observations, we propose a camera-only pipeline that combines photorealistic Gaussian Splatting with physics-based material assignment (Fig. 1). This approach enables accurate sensor simulation by integrating semantic material information into visually realistic reconstructions.

Our main **contributions** are:

- (1) A modular, camera-only pipeline integrating Gaussian Splatting for photorealistic geometry reconstruction with automated mesh-based material assignment.
- (2) An automated method for projecting 2D semantic material masks onto 3D mesh surfaces through Gaussian Splatting-based reconstruction, enabling accurate physics-based LiDAR reflectivity simulation.
- (3) Comprehensive evaluation demonstrating sensor simulation accuracy comparable to LiDAR-camera fusion, validated through LiDAR reflectivity and rendering quality analysis.

While our pipeline requires only camera input, we validate it using LiDAR ground truth from an instrumented test vehicle.

^{*}Equal contribution.

¹Siemens Digital Industries Software, 3001 Leuven, Belgium. Email: {silva.joao, son.tong}@siemens.com

²Dept. of Cognitive Robotics, Delft University of Technology, 2628 CD Delft, The Netherlands. Email: {a.huynh, H.Caesar}@tudelft.nl

This work is part of the ROBUSTIFAI project (grant agreement No. 101212818) and the SYNERGIES project (grant agreement No. 101146542), both funded by Horizon Europe – the Framework Programme for Research and Innovation. The work also benefited from two Flanders Innovation & Entrepreneurship – VLAIO funded projects: SATISFY.AI and BECAREFUL. The instrumented test vehicle was developed as part of the BECAREFUL project.

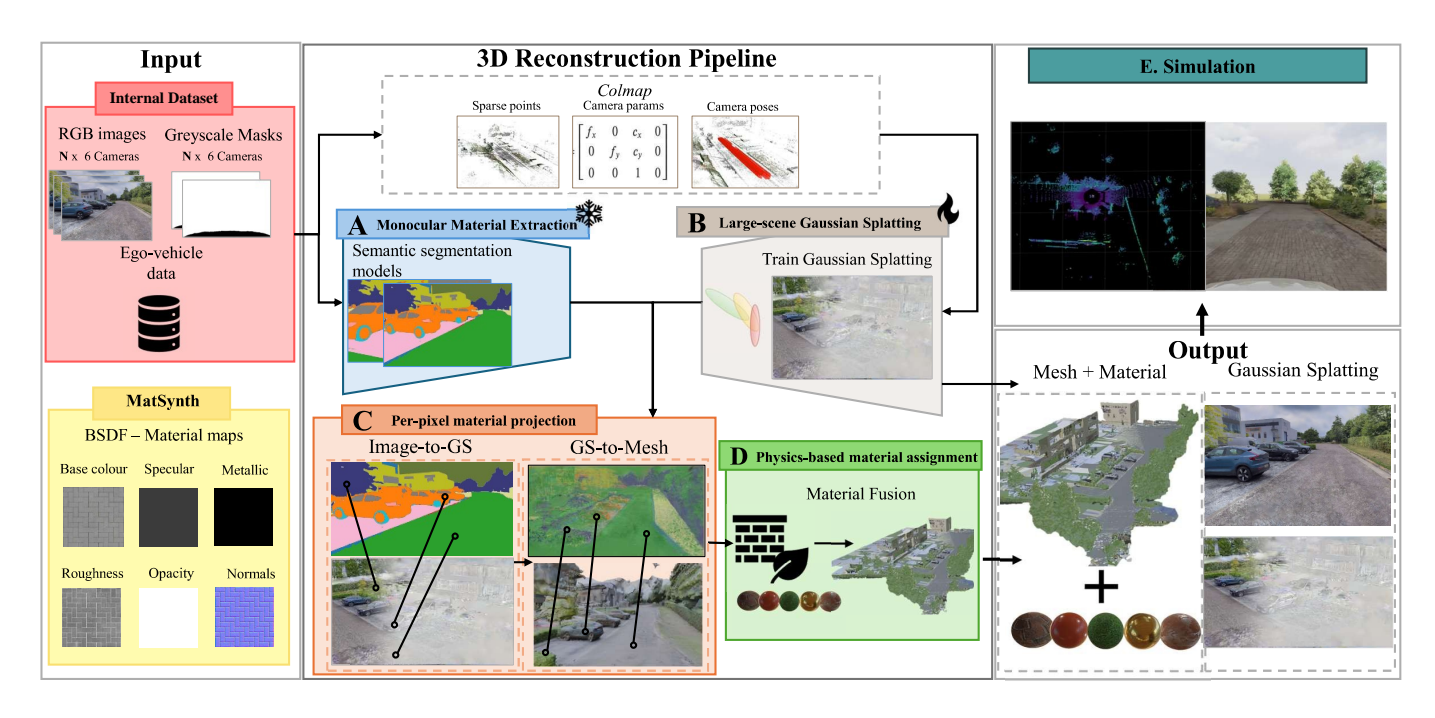


Fig. 1. Overview of our camera-only reconstruction pipeline. From RGB images, we: (a) extract semantic material masks, (b) reconstruct the 3D scene, (c) project material labels onto mesh surfaces, (d) assign physics-based materials, and (e) validate through sensor simulation.

II. RELATED WORK

A. Novel View Synthesis

Traditional 3D reconstruction methods use explicit representations. LiDAR-based methods [11] excel at geometric accuracy but struggle with fine visual details. Camera-based alternatives [23] offer richer visual information but produce noisier geometry and face challenges with transparent and reflective surfaces [22]. Neural Radiance Fields (NeRF) [18] enabled photorealistic novel view synthesis from camera-only input but suffers from high computational overhead and lacks discrete surface representation needed for graphics engines.

3D Gaussian Splatting [12] addressed these limitations through an explicit point-based representation enabling real-time rendering with photorealistic quality. Subsequent refinements have improved geometric accuracy, transparency handling, and shading [10, 36, 30]. However, these methods remain primarily oriented toward small, object-centric captures and struggle with large-scale outdoor scenes.

B. Large-Scale Scene Reconstruction

To scale Gaussian Splatting to large-scale outdoor environments, recent methods have adopted scene partitioning strategies [25], dividing scenes into spatially consistent blocks for parallel reconstruction [16, 13]. Many employ Level-of-Detail (LoD) techniques, allocating higher resolution to nearby regions to improve rendering speed. Alternative strategies include temporal segmentation [5] and distance-based decomposition [24]. However, these methods often require manual parameter tuning and lack robust surface representations needed for simulation engines.

C. Surface Extraction from Gaussian Primitives

While Gaussian Splatting enables high-quality rendering, simulation engines require explicit mesh representations. Methods such as [7] use Poisson reconstruction, while Signed Distance Field (SDF)-based approaches [4] require dense multi-view data. Recent work [8] integrates mesh extraction directly into training via Delaunay triangulation, enabling joint optimization of appearance and geometry. However, these methods are primarily designed for controlled, object-centric scenarios and lack robustness for large-scale outdoor environments.

D. Material Extraction

Beyond extracting accurate geometry, material properties are essential for realistic simulation. Image-based methods classify materials through semantic segmentation [2]. Multimodal approaches [15] and large-scale datasets [26] have improved accuracy. While LiDAR-based methods [19, 28] measure physical properties directly, camera-only approaches capture materials that LiDAR struggles with, such as transparent and reflective surfaces. However, transferring 2D material segmentation to 3D reconstructed surfaces remains challenging for camera-only Gaussian Splatting pipelines, where material labels must be accurately projected from multi-view observations onto extracted mesh geometry. Our work addresses this gap by introducing an automated projection method that enables physics-based sensor simulation.

E. Physics-Based Materials for Rendering

Once material labels are assigned to 3D surfaces, they must be represented in a format compatible with physics-based



Fig. 2. Shape-aware material refinement. From left to right: input RGB image, RMSNet predictions, FastSAM object boundaries, and final result after majority voting. The combination produces consistent material labels with sharp edges. Example from our internal dataset.

rendering engines. Modern graphics engines simulate surface interactions through the Bidirectional Reflectance Distribution Function (BRDF) [14]. Recent work integrates material properties directly into 3D Gaussians [33, 32] focusing on rendering, while mesh-compatible approaches [31] enable seamless integration with standard simulation engines. However, bridging the gap between semantic material labels from 2D segmentation and physically accurate material parameters for physics-based sensor simulation in Digital Twin environments remains an open challenge.

III. METHOD

Our pipeline reconstructs large-scale outdoor scenes from multi-view RGB images and assigns physics-based materials for accurate sensor simulation. The approach is *decoupled*, separating geometric reconstruction from material assignment, and employs a *hybrid representation*, combining photorealistic Gaussian Splatting with explicit mesh geometry. As illustrated in Fig. 1, the pipeline consists of five stages: monocular material extraction (Sec. III-A), Gaussian Splatting reconstruction (Sec. III-B), per-pixel material projection from 2D to 3D (Sec. III-C), physics-based material assignment (Sec. III-D), and simulation validation (Sec. III-E).

A. Monocular Material Extraction

We extract per-pixel material labels from RGB images using a two-stage approach: texture-based material segmentation followed by shape-aware refinement. For the first stage, we adopt RMSNet [2] due to its strong performance on autonomous driving datasets and its ability to operate on RGB images alone, without requiring LiDAR or infrared sensors. It distinguishes classes such as asphalt, concrete, glass, and metal.

However, material regions often exhibit fragmented spatial distributions and lack the prominent shape cues of semantic objects. To address this, we employ Fast Segment Anything (FastSAM) [37] to identify all instances within each scene. FastSAM produces pixel-wise boundaries, which we post-

process to remove overlaps before overlaying with RMSNet predictions.

For each segmented region, we apply majority voting: we count the material class labels within its boundary and assign the most frequent label to all enclosed pixels. This strategy ensures consistent material assignment while preserving sharp boundaries, as illustrated in Fig. 2. The result is a set of n shape-aware material masks, where each pixel inherits its class according to the FastSAM-derived segmentation.

B. Large-Scale Gaussian Splatting

Our 3D reconstruction combines photorealistic rendering with explicit geometry through a hybrid approach. We first apply COLMAP [23] to generate a sparse point cloud from multiview RGB images, providing GPS-derived camera poses, precalibrated intrinsics, and extrinsics as priors. To avoid artifacts from the moving ego-vehicle, we mask it out in all input images.

From this COLMAP output, we train two complementary models. For photorealistic visualization, we employ H3DGS [13], selected over alternatives such as CityGaussianV2 [16] due to its superior visual quality on street-level autonomous driving datasets. H3DGS constructs a global scaffold and subdivides the scene into chunks. However, its hierarchical level-of-detail representation and anti-aliasing mechanisms are not compatible with the standard format needed for downstream applications. We therefore disable these features and perform a custom merging of the chunks.

For mesh geometry and semantic labeling, we employ MiLO [8], which provides geometrically accurate mesh extraction required for physics-based simulation. Trained on the same COLMAP sparse point cloud, MiLO produces both a 3D Gaussian model and an explicit mesh. The MiLO Gaussian model initializes our semantic Gaussian Splatting for material projection (Sec. III-C), while the mesh provides the geometric basis for physics-based simulation (Sec. III-E). Both H3DGS and MiLO reconstructions share the same coordinate system, ensuring alignment between appearance and geometry.

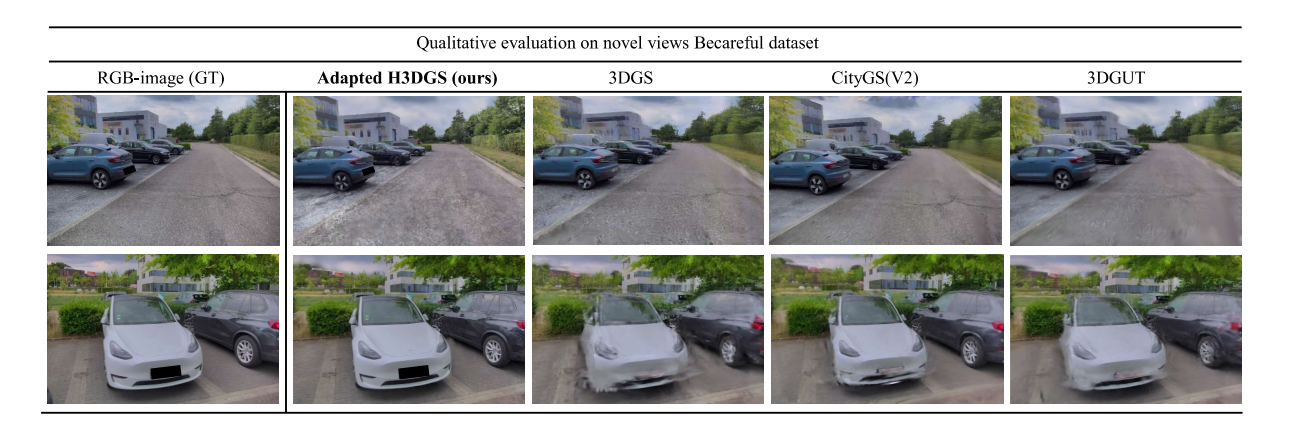


Fig. 3. Qualitative comparison of novel view rendering. From left to right: ground truth RGB, our adapted H3DGS model, 3DGS, CityGaussianV2, and 3DGUT. Our model achieves competitive visual quality comparable to state-of-the-art baselines.

C. Per-Pixel Material Projection

This module projects the 2D material masks from Sec. III-A onto the MiLO Gaussian representation, then transfers the labels to the mesh. Unlike previous pipelines relying on camera-to-LiDAR transformations, our Gaussian model is natively aligned in world coordinates. We employ differentiable rasterization [38] to render Gaussians to 2D, maintaining correspondence between 3D Gaussian positions and 2D pixel coordinates. When multiple Gaussians project to the same pixel, depth sorting during alpha blending assigns the label of the closest Gaussian.

Inconsistencies across views, such as static objects receiving different labels, are resolved using SegAnyGS [3], which enforces consistent assignment of our material masks to the Gaussians. We apply majority voting across overlaid masks to ensure label consistency. Each material-labeled Gaussian is assigned to its nearest mesh triangle using K-Nearest Neighbors (KNN), and the triangle inherits the Gaussian's label, producing a per-triangle material mesh as the final output.

D. Physics-Based Material Assignment

We assign physics-based material properties to the mesh using the Principled BSDF (Bidirectional Scattering Distribution Function) shader following the Disney BSDF standard [1], ensuring compatibility with graphics engines such as Blender, Unreal Engine, and simulation platforms like Simcenter Prescan. The Principled BSDF is parameterized by physically meaningful properties including base color, roughness, metallic factor, and transparency, ensuring physically accurate and consistent material representation.

Materials are sourced from the Matsynth dataset [27], which provides over 4,000 physically-based materials across 14 categories. These datasets provide PBR (Physically-Based Rendering) texture maps including base color, normal maps, roughness, and metallic maps. For each material class from Sec. III-A, we select representative PBR textures and apply them to the corresponding mesh triangles, producing a fully textured mesh directly usable by standard graphics engines and physics-based sensor simulation frameworks.

E. Simulation Validation

To validate our material-informed reconstruction pipeline, we integrate the reconstructed scenes into Simcenter Prescan to recreate realistic traffic scenarios with physics-based sensor simulation. The material-labeled mesh from Sec. III-D is imported into Prescan, where laboratory-measured PBR material properties are assigned to each triangle based on its material label. This enables accurate interaction with physics-based sensors, particularly LiDAR, where surface reflectivity depends on material composition.

We replicate the original sensor configuration from our instrumented test vehicle, including LiDAR specifications and mounting positions. The ego-vehicle trajectory is extracted and imported via the Simcenter Prescan MATLAB API, ensuring the virtual sensor follows the exact path and poses as during real-world data capture. The simulation generates synthetic LiDAR point clouds with material-specific reflectivity values for each point.

We validate our camera-only reconstruction by comparing these simulated LiDAR responses against real-world LiDAR measurements from the instrumented test vehicle. This demonstrates that our pipeline produces 3D models suitable for physics-based sensor simulation, providing a practical alternative to traditional LiDAR-based reconstruction workflows while achieving comparable sensor simulation accuracy.

IV. EXPERIMENTS

We evaluate our camera-only reconstruction pipeline using our internal dataset. To assess whether camera-only reconstruction achieves sensor simulation accuracy comparable to LiDAR-based methods, we establish a LiDAR-camera fusion baseline that combines LiDAR-based mesh reconstruction (NKSR [11]) with camera-derived material labels. This baseline provides geometric accuracy through direct depth measurements while incorporating semantic material information from camera images.

We conduct two complementary evaluations with different baselines: (1) visual quality, where we compare our Gaussian

TABLE I IMAGE SIMILARITY METRICS (PSNR \uparrow , SSIM \uparrow , LPIPS \downarrow) EVALUATED ON NOVEL VIEWS FOR ALL BASELINES.

	Adapted H3DGS (Ours)			3DGS			CityGaussianV2			3DGUT		
	PSNR ↑	SSIM↑	LPIPS↓	PSNR↑	SSIM↑	LPIPS↓	PSNR↑	SSIM↑	LPIPS↓	PSNR↑	SSIM↑	LPIPS↓
Scene 1	16.88	0.299	0.451	19.13	0.476	0.438	20.36	0.486	0.480	19.97	0.465	0.517
Scene 2	17.86	0.358	0.432	19.81	0.525	0.474	20.79	0.526	0.522	21.16	0.505	0.512
Scene 3	18.35	0.375	0.437	19.48	0.515	0.492	20.42	0.524	0.540	21.10	0.502	0.557
Scene 4	19.03	0.504	0.439	20.88	0.659	0.450	21.15	0.676	0.483	21.85	0.666	0.526
Scene 5	19.21	0.503	0.427	21.04	0.650	0.446	21.63	0.690	0.499	22.04	0.662	0.520
Average	18.27	0.41	0.44	20.07	0.57	0.46	20.87	0.58	0.50	21.22	0.56	0.53

Best performance highlighted in red, second-best in yellow.

Splatting reconstruction against state-of-the-art camera-only methods (3DGS [12], 3DGUT [30], CityGaussianV2 [16]) using image similarity metrics (PSNR, SSIM, LPIPS), and (2) sensor simulation accuracy, where we compare our camera-only approach against the LiDAR-camera fusion baseline by evaluating synthetic LiDAR reflectivity against real-world ground truth.

A. Dataset

We collected data using an instrumented test vehicle equipped with an Ouster OS1-128 LiDAR, six surround-view cameras, and RTK-GPS, all hardware-synchronized at 20Hz. Five static road scenes were captured in an urban environment, each approximately eight seconds long, recorded from a moving ego-vehicle.

B. Baseline

Visual quality: We compare our Gaussian Splatting reconstruction against three state-of-the-art camera-only methods: 3DGS [12], 3DGUT [30], and CityGaussianV2 [16]. All methods are trained on the same five scenes and evaluated on 50 uniformly sampled novel viewpoints per scene using PSNR, SSIM, and LPIPS.

Sensor simulation accuracy: We compare our camera-only reconstruction against a LiDAR-camera fusion baseline by simulating both environments in Simcenter Prescan with identical PBR material properties and ego-vehicle trajectories. The LiDAR-based baseline uses NKSR [11] for mesh reconstruction from LiDAR point clouds, combined with the same camera-derived material labels as our camera-only approach. This controlled setup minimizes external variables, allowing direct comparison of geometric reconstruction quality and its impact on reflectivity accuracy.

C. Implementation Details

Scene reconstruction: We train all Gaussian Splatting methods using their default hyperparameters. Material assignment follows the pipeline described in Sec. III-A–III-D, projecting semantic labels onto the reconstructed geometry and mapping them to PBR material properties.

LiDAR simulation: We configure the Simcenter Prescan Li-DAR sensor according to the specifications of the Ouster OS1-128 [20] used in our dataset. The physics-based sensor returns both Cartesian coordinates of detected points and a power value representing reflected signal strength. We normalize this power output for range and incidence angle to obtain accurate surface reflectivity values, following established calibration procedures [9].

Hardware: All experiments were conducted on a Dell Precision 7680 equipped with 64GB RAM and an NVIDIA RTX A4000 ADA Laptop GPU. Sensor validation was performed using Simcenter Prescan 2411, with scenario control via the Prescan MATLAB API (R2023b).

D. Metrics

We employ complementary metrics for visual quality and sensor simulation accuracy:

Visual quality: PSNR [6] (pixel-level fidelity), SSIM [29] (structural similarity), and LPIPS [35] (perceptual quality). Higher is better for PSNR and SSIM; lower is better for LPIPS. LiDAR simulation accuracy: Mean Absolute Error (MAE) and median error quantify reflectivity prediction error between synthetic and real-world measurements, with median providing robustness against outliers.

E. Visual Quality Evaluation

We evaluate our adapted H3DGS model against three stateof-the-art Gaussian Splatting methods by comparing novel view renderings across all five scenes.

Qualitative analysis. Figure 3 demonstrates that our adapted model achieves competitive visual quality with minimal deviation from ground truth. The model effectively fills masked ego-vehicle regions and produces cleaner reconstructions by filtering sensor noise in the ground truth. However, limitations emerge when reconstructing highly reflective and transparent surfaces, occasionally resulting in misalignments with ground truth. Rendering quality is highest for front-facing cameras, while side cameras exhibit reduced quality due to motion blur from the vehicle's movement. Scenes with dense object distributions and occlusions also reduce reconstruction quality. Quantitative analysis. Table I presents PSNR, SSIM, and LPIPS metrics across all methods and scenes. Our adapted model achieves lower PSNR (18.27 vs. 20.07-21.22) and SSIM (0.41 vs. 0.56–0.58) compared to baselines. However, it achieves the best average LPIPS score (0.44 vs. 0.46–0.53),

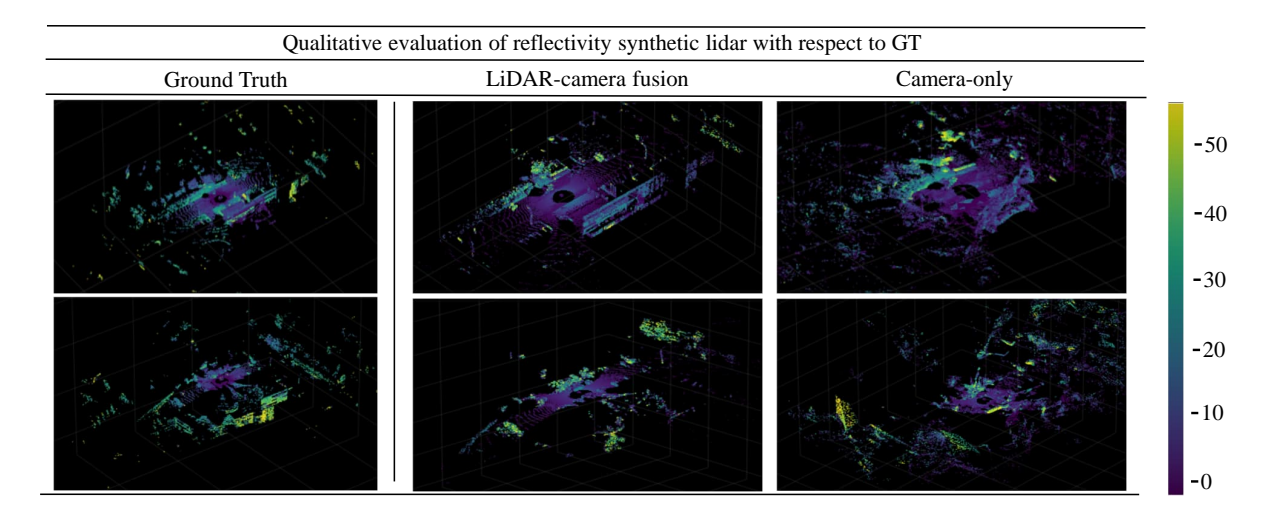


Fig. 4. From left to right: real-world LiDAR ground truth from our instrumented vehicle, LiDAR-camera fusion baseline simulated in Prescan, and our camera-only reconstruction simulated in Prescan.

outperforming all methods on four out of five scenes. This is particularly significant since LPIPS correlates strongly with human perceptual similarity [35], suggesting that our reconstruction maintains perceptual quality despite lower pixel-level accuracy. The lower PSNR and SSIM values potentially stem from our architectural modifications: disabling H3DGS's hierarchical level-of-detail representation and anti-aliasing mechanisms (Sec. III-B) trades pixel-level accuracy for compatibility with downstream simulation engines. However, the superior LPIPS score suggests that these modifications preserve perceptual quality.

F. LiDAR Simulation Accuracy

We evaluate our camera-only Gaussian Splatting reconstruction against the LiDAR-camera fusion baseline by measuring reflectivity error relative to real-world ground truth.

TABLE II
LIDAR REFLECTIVITY PREDICTION ERROR (LOWER IS
BETTER). REFLECTIVITY VALUES NORMALIZED TO 0–255
RANGE.

	Camera-	only (Ours)	LiDAR-based		
	MAE↓	Median↓	MAE↓	Median↓	
Scene 1	10.91	7.16	11.73	7.84	
Scene 2	9.37	5.54	10.17	6.70	
Scene 3	11.03	6.91	10.47	6.87	
Scene 4	9.32	5.77	9.41	6.02	
Scene 5	8.98	6.71	8.76	6.36	
Average	10.05	6.48	10.14	6.78	

MAE: Mean Absolute Error. Our camera-only method achieves comparable accuracy to the LiDAR-based base-line

Qualitative analysis. Figure 4 presents a visual comparison of LiDAR reflectivity predictions between our camera-only method, the LiDAR-camera fusion baseline, and real-world

ground truth. Both methods exhibit reflectivity errors, with vegetation consistently showing higher predicted reflectivity than ground truth—likely due to the diversity of vegetation forms and our simplified PBR material parameterization. The camera-only reconstruction exhibits more geometric noise than the LiDAR-based approach, as expected from camera-based methods. Despite these differences, both simulation approaches produce comparable reflectivity patterns, validating our camera-only pipeline for sensor simulation applications.

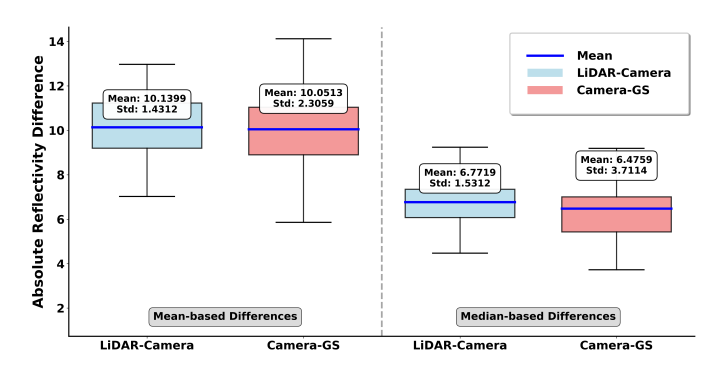


Fig. 5. Distribution of absolute reflectivity errors for camera-only (ours) and LiDAR-based reconstruction methods. Our camera-only approach achieves comparable median error with slightly higher variability.

Quantitative analysis. Table II and Figure 5 present reflectivity error metrics across all five scenes. Our camera-only method achieves comparable reflectivity accuracy to the LiDAR-camera fusion baseline, with mean absolute error (MAE: 10.05 vs. 10.14) and median error (6.48 vs. 6.78) showing minimal differences between the two approaches. This demonstrates that camera-only reconstruction can achieve sensor simulation accuracy comparable to LiDAR-based methods without requiring LiDAR hardware or complex sensor synchronization. The higher within-scene variability in camera-only results (visible in Figure 5) reflects the increased geo-

metric noise inherent to camera-based reconstruction, which lacks the direct depth measurements provided by LiDAR.

G. Ablation Study

We evaluate the impact of incorporating segmentation masks to improve material classification accuracy. As described in Sec. III-A, we augment RMSNet's material predictions with shape cues from segmentation models.

Experimental setup. We quantitatively assess segmentation quality using the MCubes multi-modal dataset [15], which contains 500 material-annotated images. We compare three configurations: (1) RMSNet alone, (2) RMSNet + FastSAM, and (3) RMSNet + SAM2 [21].

TABLE III

MATERIAL SEGMENTATION PERFORMANCE ON

MCUBES DATASET [15].

Method	Accuracy	mIoU
RMSNet	0.63	0.28
RMSNet + FastSAM (Ours)	0.65	0.29
RMSNet + SAM2	0.67	0.31

Results. Table III shows that adding segmentation masks improves both accuracy (from 0.63 to 0.65–0.67) and mIoU (from 0.28 to 0.29–0.31) over RMSNet alone. While SAM2 achieves the highest scores (0.67 accuracy, 0.31 mIoU), we select FastSAM (0.65 accuracy, 0.29 mIoU) due to its significantly lower computational cost and faster inference speed—critical for processing large-scale multi-view datasets. Although SAM2 offers superior segmentation quality, the 2% accuracy improvement does not justify the increased computational overhead for our application.

Analysis. The 3.2% accuracy improvement (0.63 to 0.65) demonstrates that shape cues effectively enhance material classification consistency. However, segmentation masks can occasionally reduce per-pixel accuracy when incorrect predictions propagate across larger regions, potentially overwriting fine details such as road markings. The 2% accuracy gap between FastSAM and SAM2 (0.65 vs. 0.67) represents an acceptable tradeoff for the practical benefits of automatic mask extraction in large-scale scenarios.

V. CONCLUSION

We present a camera-only pipeline that combines photorealistic Gaussian Splatting with physics-based material assignment for Digital Twin reconstruction. Our approach leverages Gaussian Splatting to bridge 2D camera observations to comprehensive 3D scene representations, including photorealistic visuals, semantic information, mesh geometry, and material properties for sensor simulation. Through comprehensive evaluation on real-world urban driving scenes using LiDAR ground truth for validation, we demonstrate that our material projection approach achieves reflectivity prediction accuracy comparable to LiDAR-based methods while maintaining photorealistic rendering quality, offering a practical alternative for ADAS development when LiDAR is unavailable or impractical.

Future work. Future directions include improving geometric reconstruction quality from camera inputs, extending to dynamic scenes, and exploring learned material representations to reduce dependency on predefined PBR databases.

REFERENCES

- [1] B. Burley and Walt Disney Animation Studios. Physically-based shading at disney. In *ACM SIGGRAPH*, 2012.
- [2] S. Cai, R. Wakaki, S. Nobuhara, and K. Nishino. Rgb road scene material segmentation. In *ACCV*, 2022.
- [3] J. Cen, J. Fang, C. Yang, L. Xie, X. Zhang, W. Shen, and Q. Tian. Segment any 3d gaussians, 2025.
- [4] H. Chen, C. Li, Y. Wang, and G. H. Lee. Neusg: Neural implicit surface reconstruction with 3d gaussian splatting guidance, 2025.
- [5] X. Cui, W. Ye, Y. Wang, G. Zhang, W. Zhou, and H. Li. Streetsurfgs: Scalable urban street surface reconstruction with planar-based gaussian splatting, 2024.
- [6] R. C. Gonzalez and R. E. Woods. *Digital Image Processing*. Pearson, 3rd edition, 2008.
- [7] A. Guédon and V. Lepetit. Sugar: Surface-aligned gaussian splatting for efficient 3d mesh reconstruction and high-quality mesh rendering. In *CVPR*, 2024.
- [8] A. Guédon, D. Gomez, N. Maruani, B. Gong, G. Drettakis, and M. Ovsjanikov. Milo: Mesh-in-the-loop gaussian splatting for detailed and efficient surface reconstruction, 2025.
- [9] N. Hermidas and M. Phillips. Physics based lidar power calibration. Technical report, Siemens Industry Software Netherlands B.V., May 2021.
- [10] B. Huang, Z. Yu, A. Chen, A. Geiger, and S. Gao. 2d gaussian splatting for geometrically accurate radiance fields. In *SIGGRAPH*, July 2024.
- [11] J. Huang, Z. Gojcic, M. Atzmon, O. Litany, S. Fidler, and F. Williams. Neural kernel surface reconstruction. In CVPR, 2023.
- [12] B. Kerbl, G. Kopanas, T. Leimkühler, and G. Drettakis. 3d gaussian splatting for real-time radiance field rendering, 2023.
- [13] B. Kerbl, A. Meuleman, G. Kopanas, M. Wimmer, A. Lanvin, and G. Drettakis. A hierarchical 3d gaussian representation for real-time rendering of very large datasets. ACM TOG, 43(4), July 2024.
- [14] M. Kurt. A survey of bsdf measurements and representations. *J. Sci. Eng.*, 20(58), 2018.
- [15] Y. Liang, R. Wakaki, S. Nobuhara, and K. Nishino. Multimodal material segmentation. In *CVPR*, June 2022.
- [16] Y. Liu, C. Luo, Z. Mao, J. Peng, and Z. Zhang. City-gaussianv2: Efficient and geometrically accurate reconstruction for large-scale scenes, 2025.
- [17] S. Manivasagam, S. Wang, K. Wong, W. Zeng, M. Sazanovich, S. Tan, B. Yang, W.-C. Ma, and R. Urtasun. Lidarsim: Realistic lidar simulation by leveraging the real world, 2020.

- [18] B. Mildenhall, P. P. Srinivasan, M. Tancik, J. T. Barron, R. Ramamoorthi, and R. Ng. Nerf: Representing scenes as neural radiance fields for view synthesis, 2020.
- [19] Stefan Muckenhuber, Hannes Holzer, and Zrinka Bockaj. Automotive lidar modelling approach based on material properties and lidar capabilities. *Sensors*, 20(11):3309, 2020.
- [20] Ouster, Inc. Os1 lidar sensor specifications, 2024.
- [21] N. Ravi, V. Gabeur, Y.-T. Hu, R. Hu, C. Ryali, T. Ma, H. Khedr, R. Rädle, C. Rolland, L. Gustafson, E. Mintun, J. Pan, K. V. Alwala, N. Carion, C.-Y. Wu, R. Girshick, P. Dollár, and C. Feichtenhofer. Sam 2: Segment anything in images and videos, 2024.
- [22] F. Remondino, A. Karami, Z. Yan, G. Mazzacca, S. Rigon, and R. Qin. A critical analysis of nerf-based 3d reconstruction. *Remote Sens.*, 15(14), 2023.
- [23] J. L. Schönberger and J.-M. Frahm. Structure-frommotion revisited. In CVPR, 2016.
- [24] X. Shi, L. Chen, P. Wei, X. Wu, T. Jiang, Y. Luo, and L. Xie. Dhgs: Decoupled hybrid gaussian splatting for driving scene, 2024.
- [25] M. Tancik, V. Casser, X. Yan, S. Pradhan, B. Mildenhall, P. P. Srinivasan, J. T. Barron, and H. Kretzschmar. Blocknerf: Scalable large scene neural view synthesis, 2022.
- [26] P. Upchurch and R. Niu. A dense material segmentation dataset for indoor and outdoor scene parsing, 2022.
- [27] G. Vecchio and V. Deschaintre. Matsynth: A modern pbr materials dataset. In *CVPR*. IEEE, June 2024.
- [28] K. Viswanath, P. Jiang, and S. Saripalli. Reflectivity is all you need!: Advancing lidar semantic segmentation, 2024.
- [29] Z. Wang, A. C. Bovik, H. R. Sheikh, and E. P. Simon-celli. Image quality assessment: from error visibility to structural similarity. *IEEE TIP*, 13(4), 2004.
- [30] Q. Wu, J. Martinez Esturo, A. Mirzaei, N. Moenne-Loccoz, and Z. Gojcic. 3dgut: Enabling distorted cameras and secondary rays in gaussian splatting. In CVPR, 2025.
- [31] B. Xiong, J. Liu, J. Hu, C. Wu, J. Wu, X. Liu, C. Zhao, E. Ding, and Z. Lian. Texgaussian: Generating highquality pbr material via octree-based 3d gaussian splatting. In CVPR, June 2025.
- [32] Y. Yao, Z. Zeng, C. Gu, X. Zhu, and L. Zhang. Reflective gaussian splatting, 2025.
- [33] J. Ye, L. Zhu, R. Zhang, Z. Hu, Y. Yin, L. Li, L. Yu, and Q. Liao. Large material gaussian model for relightable 3d generation, 2025.
- [34] J. E. Zaalberg. Reducing the sim-to-real gap: Lidar-based 3d static environment reconstruction. Master's thesis, TU Delft, 2024.
- [35] R. Zhang, P. Isola, A. A. Efros, E. Shechtman, and O. Wang. The unreasonable effectiveness of deep features as a perceptual metric, 2018.
- [36] Z. Zhang, B. Huang, H. Jiang, L. Zhou, X. Xiang, and S. Shen. Quadratic gaussian splatting for efficient and detailed surface reconstruction, 2024.
- [37] X. Zhao, W. Ding, Y. An, Y. Du, T. Yu, M. Li, M. Tang,

- and J. Wang. Fast segment anything, 2023.
- [38] M. Zwicker, H. Pfister, J. Van Baar, and M. Gross. Ewa volume splatting. In *IEEE Vis.* IEEE, 2001.